**Correspondence to:**
T. Gulyaeva,
gulyaeva@izmiran.ru

# Generation of Proxy GIM-TEC for Extreme Storms Before the Era of GNSS Observations

**Tamara Gulyaeva[1] , Valentin Shubin[1] , Haris Haralambous[2], Manuel Hernández-Pajares[3] , and Iwona Stanislawska[4]**

[1]IZMIRAN, Moscow, Russia, [2]Frederick Research Center, Nicosia, Cyprus, [3]Universitat Politecnica de Catalunya (UPC), Barcelona, Spain, [4]Space Research Centre PAS, Warsaw, Poland

**Abstract** For the first time, we reconstructed global distribution of both the total electron content disturbance W index and TEC values for eight extreme storms (Dst $< -250$ nT) occurred before the epoch of GNSS observations in solar cycle 22. We created a model based on superposed epoch analysis of the training set of GIM-W maps of nine SC23 extreme storms. Global GIM-W index maps are calculated from 15-min UPC GIM-TEC (UQRG) as the logarithmic deviation of instantaneous TEC from the monthly median GIM-MTEC empirical model. We introduced the storm phase metrics for main and recovery phases of the positive ionosphere disturbance (the WU-index), the negative disturbance (the WL-index) and the ring current (the Dst-index). The probabilistic forecasting model (Pmodel) for SC22 GIM-W$_x$ maps is developed based on GIM-W maps of the SC23 training set. The storm phase distribution $\Phi_x$ for the eight SC22 extreme storms is calculated from the proxy time shift (lag) of peak WU$_{max}$ and WL$_{min}$ relative to Dst$_{min}$. Proxy GIM-TEC$_x$ maps are calculated by adjusting the GIM-MTEC median to the GIM-W$_x$ prediction. Validation of the technique based on data of UPC and JPL for four intense ionospheric storms showed a root-mean-square error less than 3 TECU. The proposed technique can be applied for both the past and future forecasting of GIM-W index and GIM-TEC maps.

## 1. Introduction

Total Electron Content (TEC) in the Earth's ionosphere and plasmasphere is a reliable indicator of the impact of long-term and short-term changes on the Sun, the interplanetary space and the Earth's upper atmosphere. Therefore, the development of TEC models are of great importance in today's space weather science and applications. Currently, climate models of the ionosphere and methods for forecasting the ionospheric disturbances are being successfully developed based on the analysis of TEC and Global Ionosphere Maps (GIM-TEC) from GNSS observations during 23–24 solar cycles (SC). Relevant examples and references are presented in the works (Aa et al., 2012; Chen et al., 2015; Erdogan et al., 2020; Feng et al., 2019; Goncharenko et al., 2021; Gulyaeva, 1999; Ivanov et al., 2011; Jakowski et al., 2011; Lean, 2019; Lean et al., 2016; Q. Liu, Hernández-Pajares, Lyu, Nishioka, et al., 2021; Meng & Verkhoglyadova, 2021; Mukhtarov, Andonov, et al., 2013; Mukhtarov, Pancheva, et al., 2013; Ratovsky et al., 2020). The machine learning and artificial intelligence models are applied by Cesaroni et al. (2020) and L. Liu et al. (2020). There are two main approaches to forecasting TEC. On the one hand, several straightforward models for direct forecasting of TEC are based on its interrelations with the driving forces (Goncharenko et al., 2021; Lean, 2019; Lean et al., 2016) or on the previous GIM evolution (Monte Moreno et al., 2018); a second approach is based on preliminary forecasting of ionosphere variability, which is then converted to GIM-TEC calculations (Mukhtarov, Pancheva, et al., 2013). The latter approach is pursued in the present study.

Long-term 3D global models such as the IRI, IRI-Plas, NeQuick, SMI, etc., represent climate changes of the ionosphere (Bilitza et al., 2017; Chasovitin et al., 1987; Gulyaeva et al., 2013; Nava et al., 2008). The data availability for their assimilation by a model presents crucial requirement to achieve data/model agreement (Erdogan et al., 2020; Pignalberi et al., 2019). However, global total electron content data are not accessible for assimilation during pre-IGS period before the International GNSS Service and the IGS Ionospheric working group were established (Beutler et al., 2009; Feltens, 2003; Hernández-Pajares et al., 2009), that is, before SC23. No GIM-TEC forecasting technique has been applied so far for a reliable retrospective study of historical GIM-TEC storms that occurred before the era of GNSS products, similar to the study of super-storms with assimilation of the ionosonde data (Stanislawska et al., 2018). However, the data gaps in ionosonde records (in space and time), the

sporadic E and F spread phenomena, a lack of ionosondes over the oceans and other limitations and shortcomings in monitoring F2-layer peak parameters hinder the application of the ionosonde data for the global mapping of the ionosphere (Galkin et al., 2020; Shubin & Gulyaeva, 2021). The time has come to produce simulated instantaneous GIM-TEC maps for the epoch prior to GNSS observations to express past global ionosphere variations.

The purpose of this study is the development of a probabilistic forecasting model (Pmodel) for producing proxy global maps of the ionospheric index GIM-W$_x$. Based on this model, a retrospective reconstruction of hourly instantaneous GIM-TEC$_x$ maps will be made for the intense geomagnetic storms that occurred during SC22. There have been eight extreme storms with peak Dst < −250 nT observed during SC22 which we call 'modelling set'. The analysis is based on nine extreme storms of the similar intensity (Dst < −250 nT) observed during SC23 ('training set'). No major storms of Dst < −250 nT were observed during SC24 so for validating the proposed Pmodel we accept four intense storms of SC23 and SC24 with peak Dst < −200 nT ('testing set').

## 2. Analysis of Global Ionosphere Maps

High-time-resolution (including 15, 30, 45 and 60 min) maps are recommended for the application of GIMs with the highest accuracy (Gulyaeva & Mannucci, 2020; Q. Liu, Hernández-Pajares, Lyu, & Goss, 2021; Milanowska et al., 2021). In a past comparison of different GIM-TECs for high and low solar activity, the highest accuracy was obtained by the post-processed UQRG GIMs provided by the Universitat Politècnica de Catalunya (UPC) (Wielgosz et al., 2021). In order to meet the demand for real-time GIM, the UPC developed a Real-Time TOMographic IONosphere (RT-TOMION) software model and initiated the systematic generation of UPC RT-GIM on February 6, 2011 (Li et al., 2020; Q. Liu, Hernández-Pajares, Yang, et al., 2021). Both UPC RT-GIM and post-processed GIM-TEC maps (UQRG) are produced in IONEX format (Schaer, 1999) and provide a numerical representation of global TEC in the latitude ranges of 87.5°S to 87.5°N in steps of 2.5°, and a longitude ranges from 180°W to 180°E in steps of 5° with a temporal resolution of 15 min in UT (Hernández-Pajares et al., 1999, 2009; Q. Liu, Hernández-Pajares, Lyu, & Goss, 2021).

The post-processed GIM-TEC global maps (UQRG) at 15-min cadence produced by UPC since December 1996 (Orús et al., 2005; Li et al., 2020; Q. Liu, Hernández-Pajares, Yang, et al., 2021) are used in the present study to produce 15-min GIM-W maps provided by IZMIRAN (https://www.izmiran.ru/ionosphere/weather/archive/). TEC-based W-index of ionosphere variability represents the logarithmic deviation of instantaneous TEC from the observed running median TECμ for 15 preceding days at each grid point of the IONEX map (Gulyaeva et al., 2021). In producing the W-index at each cell of GIM as a logarithm of the ratio of the instantaneous TEC to the median TECμ, an occasional negative or zero TEC ≤0 value occurring sometimes at the source GIM-TEC cannot be used for the logarithm calculation. The annual occurrence of TEC ≤ 0 varies from 0.002% (2010) to 0.03% (1997, 2020). In such a case, the negative TEC value is substituted by a minimum positive proxy TEC = 0.1 TECU.

For the present study, an additional set of GIM-W maps is derived from 15-min UPC GIM-TEC in which the −15 days running median TECμ is replaced by the model MTEC median. Global median empirical MTEC model is constructed using a spherical harmonic analysis based on observed JPL GIM-TEC maps for the period 1996–2019 (Shubin & Gulyaeva, 2022), driven by a recalibrated sunspot number series SSN2 similar to the approach adopted in (Shubin & Gulyaeva, 2021). MTEC model provides prediction of median TEC for any time and space, particularly, GIM-MTEC denotes monthly-median TEC for the IONEX grids. It should be noted that the W-index relative to MTEC differs from the value that is calculated using the observed running median over the preceding 15 days (Gulyaeva et al., 2013, 2021). However, for reconstructing the unknown instantaneous GIM-TECs prior to 1996, the running −15 days median TECμ is unknown, while the MTEC model makes it possible to calculate the median for any moment of time.

The method used in our study is based on a data-driven analysis. In particular, data from extreme severe storms with Dst < −250 nT observed during SC23 are adopted as the training set of the source maps for the calculation of the GIM-W index. GIM-W indices from the training set are produced from UQRG GIM-TECs with 15-min cadence for the extreme SC23 storms listed in Table 1. Table 1 includes storm onset day and time, the time and magnitude of the Dst peak, the time and magnitude of the peak of the positive phase (WU$_{max}$), and the negative phase (WL$_{min}$), according to WU and WL indices (Gulyaeva et al., 2021). The 12-month smoothed sunspot number SSN2 is also included. Storm duration is assumed to be 48 h after the storm onset. All events considered in

**Table 1**
*Training Set of the Extreme Storms for SC23*

| Start year-mm-dd | UT | Dst$_{min}$ mm-dd | UT | Dst | WU$_{max}$ mm-dd | UT | WU | WL$_{min}$ mm-dd | UT | WL | SSN |
|---|---|---|---|---|---|---|---|---|---|---|---|
| 2000-04-06 | 17:00 | 04-07 | 00:00 | −288 | 04-06 | 20:45 | 5.11 | 04-07 | 09:15 | −5.25 | 175 |
| 2000-07-15 | 16:00 | 07-16 | 00:00 | −301 | 07-15 | 22:15 | 5.77 | 07-16 | 04:15 | −5.90 | 174 |
| 2001-03-31 | 04:00 | 03-31 | 08:00 | −387 | 03-31 | 05:15 | 2.65 | 03-31 | 23-75 | −6.29 | 155 |
| 2001-04-11 | 15:00 | 04-11 | 23:00 | −271 | 04-11 | 18:45 | 4.81 | 04-12 | 08:45 | −6.32 | 161 |
| 2001-11-06 | 02:00 | 11-06 | 06:00 | −292 | 11-06 | 04:00 | 4.55 | 11-06 | 07:15 | −5.61 | 180 |
| 2003-10-30 | 16:00 | 10-30 | 22:00 | −383 | 10-30 | 21:00 | 4.93 | 10-31 | 04:00 | −5.26 | 89 |
| 2003-11-20 | 08:00 | 11-20 | 20:00 | −422 | 11-20 | 20:00 | 4.61 | 11-21 | 00:00 | −5.24 | 87 |
| 2004-11-07 | 19:00 | 11-08 | 06:00 | −373 | 11-08 | 05:00 | 4.65 | 11-08 | 09:15 | −5.70 | 57 |
| 2005-05-15 | 03:00 | 05-15 | 08:00 | −263 | 05-15 | 08:00 | 4.27 | 05-16 | 10:45 | −5.59 | 45 |

the present study refer to periods of high solar activity (the training set, Table 1; the modeling set, Table 2; and the testing set, Table 4).

Figure 1 shows plots of the global WU-index (upper panel), the WL-index (middle panel), and the Dst-index (lower panel) for each of the nine training storms. Storm Sudden Commencement (SSC) is indicated at onset $t_0$. All ionospheric and geomagnetic parameters are plotted for the 24 h prior to the onset of each storm, $t_0$, and for the next 48 h after storm commencement. The black curves indicate the median for 9 storms, from which the WU$_{max}$ is observed earlier than Dst$_{min}$, and WL$_{min}$ is delayed regarding Dst$_{min}$.

The time lag $\Delta t$ of the two storm processes with respect to Dst$_{min}$ is expressed analytically in Gulyaeva and Mannucci (2020). Based on the expressions obtained there for the advance of the peak of the positive storms, and the lag (delay) of the peak of the negative storms relative to time $t(\text{Dst}_{min})$ and the value of Dst$_{min}$, we obtain (in hours):

$$t(\text{WU}_{max}) = t(\text{Dst}_{min}) + 0.01345 \times \text{Dst}_{min} - 0.1536 \tag{1a}$$

$$t(\text{WL}_{min}) = t(\text{Dst}_{min}) + 0.01166 \times \text{Dst}_{min} + 11.73 \tag{1b}$$

Equations 1a and 1b are used below to calculate the proxy moments $t(\text{WU}_{max})$ and $t(\text{WL}_{min})$ given in Table 2, for the reconstruction of the extreme SC22 ionosphere storms, for which the distributions of WU and WL indices are unknown and investigated in the present study.

Table 2 presents a series of eight extreme SC22 storms with Dst < −250 nT (the target model set), for which the unknown proxy maps GIM-W$_x$ and GIM-TEC$_x$ are calculated in the following analysis. This table shows the geomagnetic storm onset day and time, the time and magnitude of the Dst peak, the time of the peak of the positive phase WU$_{max}$ (Equation 1a), the peak of the negative phase WL$_{min}$ (Equation 1b), and the solar sunspot number

**Table 2**
*Modeling Set of the Extreme Storms for SC22*

| Start year-mm-dd | UT | Dst$_{min}$ mm-dd | UT | Dst | WU$_{max}$ mm-dd | UT | WL$_{min}$ mm-dd | UT | SSN |
|---|---|---|---|---|---|---|---|---|---|
| 1989-03-13 | 08:00 | 03-14 | 01:00 | −589 | 03-13 | 12:00 | 03-14 | 07:00 | 198 |
| 1989-09-18 | 11:00 | 09-19 | 04:00 | −255 | 09-18 | 19:00 | 09-19 | 13:00 | 210 |
| 1989-10-20 | 09:00 | 10-21 | 16:00 | −268 | 10-20 | 18:00 | 10-22 | 01:00 | 212 |
| 1989-11-17 | 09:00 | 11-17 | 22:00 | −266 | 11-17 | 18:00 | 11-18 | 07:00 | 212 |
| 1991-03-24 | 04:00 | 03-25 | 00:00 | −298 | 03-24 | 20:00 | 03-25 | 08:00 | 204 |
| 1991-10-28 | 11:00 | 10-29 | 07:00 | −254 | 10-29 | 03:00 | 10-29 | 16:00 | 197 |
| 1991-11-08 | 13:00 | 11-09 | 01:00 | −354 | 11-08 | 20:00 | 11-09 | 09:00 | 191 |
| 1992-05-10 | 07:00 | 05-10 | 14:00 | −288 | 05-10 | 10:00 | 05-10 | 22:00 | 142 |
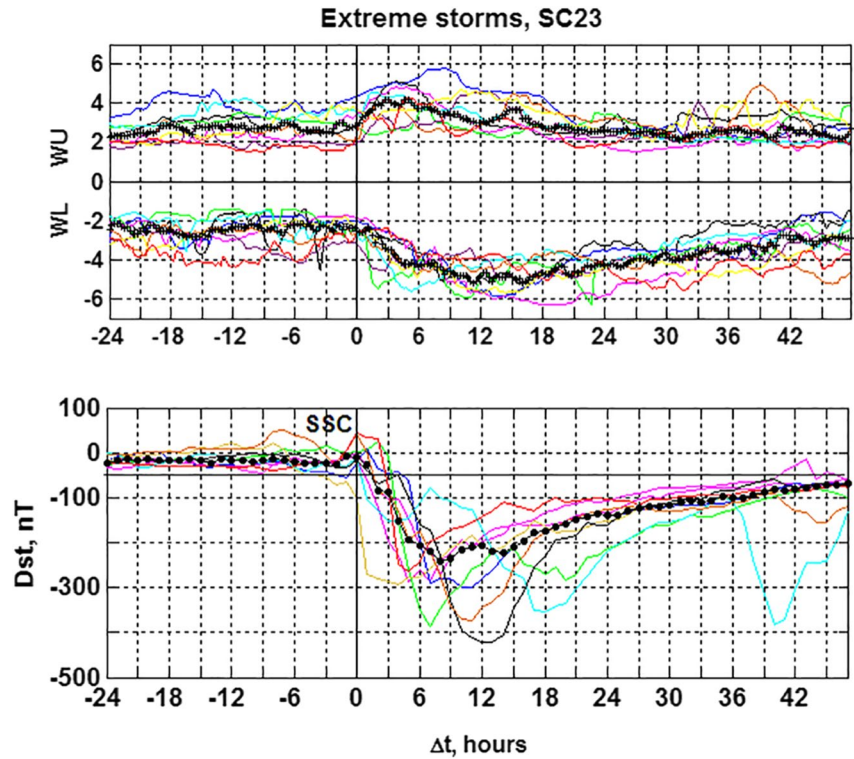
**Figure 1.** Temporal variation of the ionospheric positive storm WU index and negative storm WL index and the ring current storm Dst index and their median for nine extreme storms observed for SC23 during 24 h preceding storm onset $t_0$ and 48 h afterward.

SSN2. Target maps GIM-W$_x$ and GIM-TEC$_x$ are generated during 72 h UT (i.e., three full days) covering the time interval of $t_0$ +48 h of storm duration.

## 3. Storm Phase Probability Pmodel From SC23 Extreme Storms

To ensure homogeneity between the different storm data series, we introduce a phase portrait for ionospheric WU and WL indices, and the geomagnetic Dst-index. The main phase of the storm $\Phi$ varies in the range [0: 1] from the storm onset at $t_0$ to the storm peak (WU$_{max}$, WL$_{min}$ and Dst$_{min}$), and the recovery phase $\Phi$ varies in the range [−1: 0] after the storm peak (WU$_{max}$, WL$_{min}$ and Dst$_{min}$). We express the ionospheric indices WU($\Phi$) and WL($\Phi$), calculated from GIM-WTEC for the training set of SC23 storms (Table 1), and Dst($\Phi$) for both the SC23 training set (Table 1) and the SC22 modeling set (Table 2).

The observed WU, WL or Dst-index is represented by a series of successive values of the index during the storm: $n_i$ = 0, 1, 2,…, $n$ − 1, where $n$ is the total number of index values in the time series. In particular, for the total 2-diurnal storm period from $t_0$ to $t_{n-1}$ the time series includes $n$ = 48 index values with a latency of $\Delta t$ = 1 h and $n$ = 192 with 15-min cadence data. The number $n_m$ refers to the time of the storm peak in the series ranging from 0 to $n$ − 1. The $\Phi_i$ variation in the main phase of the storm from 0 to 1 for $n_i \leq n_m$ ($n_i$ = 0, 1, 2,…, $n_m$) is calculated as:

$$\Phi_i = n_i/n_m \tag{2a}$$

Variation of $\Phi_i$ in the recovery phase from −1 to 0 for $n_i \geq n_m$ ($n_i = n_m$, $n_{m+1}$,…, $n$ − 1) is expressed as:

$$\Phi_i = (n_i − n)/|n_m − n| \tag{2b}$$

where symbols $|$ … $|$ represent the absolute value of the expression. In the storm phase metrics, the particular values of indices WU, WL or Dst are assigned to the series of $\Phi_i$ (Equations 2a and 2b).
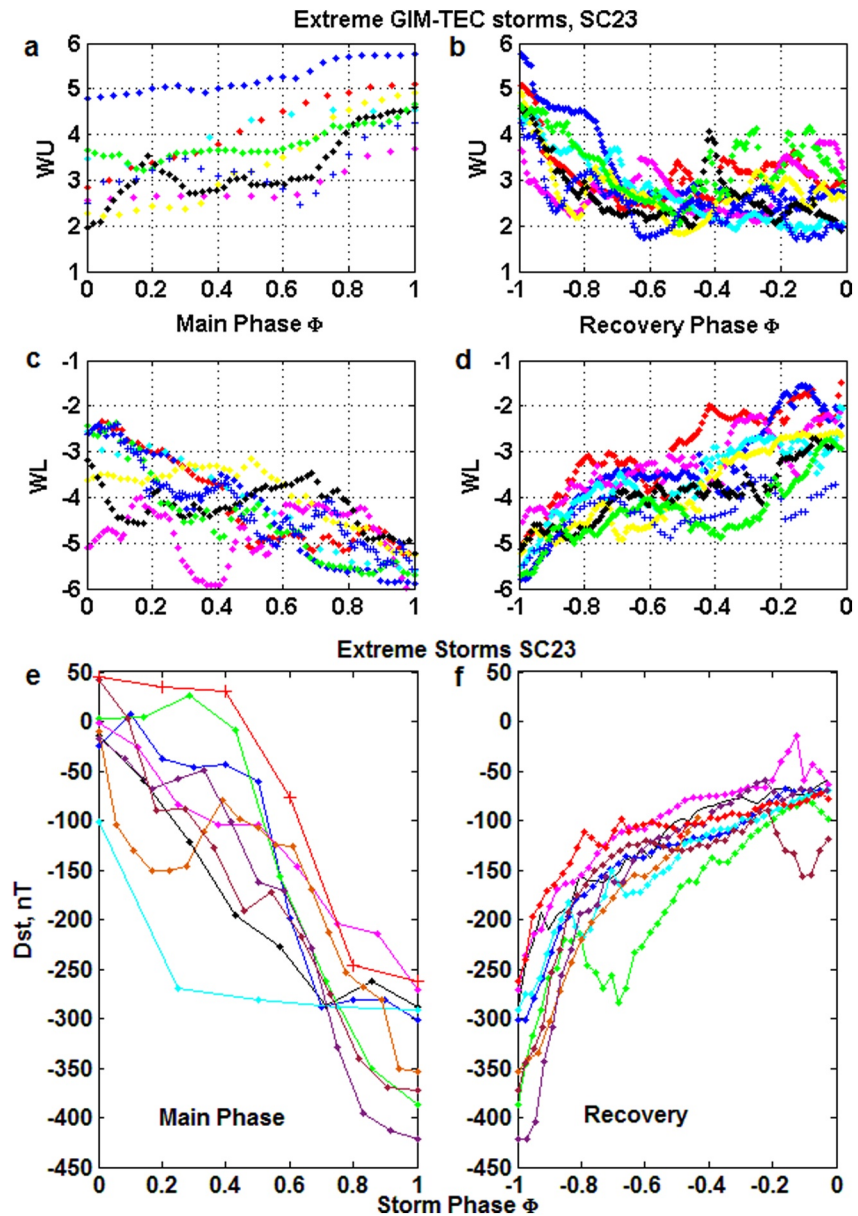
**Figure 2.** Variation of ionospheric and geomagnetic global indices against the main phase and recovery phase of nine extreme storms and their median for the training set of SC23. (a, b) WU(Φ) index; (c, d) WL(Φ) index; (e, f) Dst(Φ) index.

Variation in WU(Φ) (Figures 2a and 2b), WL(Φ) (Figures 2c and 2d) and Dst(Φ) (Figures 2e and 2f) is plotted in Figures 2a–2f for nine extreme storms of the SC23 training set. This figure illustrates a similarity in the behavior of these storms, including an increase in the positive WU-index (compared to a decrease for negative WL and Dst indices) during the main phase, and opposite trends in the recovery phase. Presentation of WU and WL indices in terms of the storm phase allows evaluating a significance of the training and testing sets of observed indices. With Student's $t$-test we obtain $t = 0.2625$ for WU data, and $t = 1.1404$ for WL data which yield probability $p = 0.134$ for WU and $p = 0.155$ for WL. The $t$-test is relatively robust to moderate violations of the normality assumption. The significance level is equal to 86.64% for WU and 84.45% for WL data sets. We assume the similar variations of the ionosphere during the severe storms of SC22.

Although the variation of WU(Φ) and WL(Φ) for the SC22 modeling set remains unknown, it is possible to calculate variation of the phase Φ for the main and recovery phases using Equations 2a and 2b, taking account of the shift (lag) of the peak of these parameters with respect to the Dst peak (Equations 1a, 1b; Table 2). Figure 3
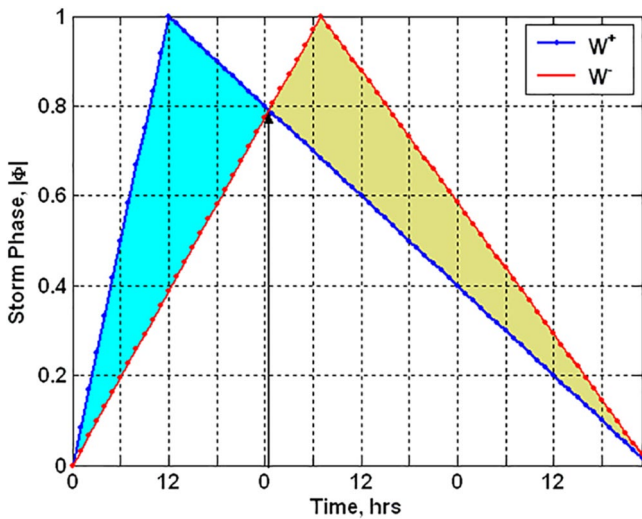
**Figure 3.** Time variation of an absolute value of storm phase $|\Phi_x|$ for the modeling positive ionosphere storm (W⁺) and negative ionosphere storm (W⁻) during 3 days of the super-storm on March 13–15, 1989.

shows a plot of absolute values of the storm phase $|\Phi_x|$ during the course of three days for the super-storm on March 13–15, 1989, which proves to be a 100-year event (Love et al., 2015). The symbol '$x$' is assigned to the parameter in the SC22 modeling set. We observe that the peak $\Phi_x = 1$ of the positive $WU_x$ index happens before the peak $\Phi_x = -1$ of the negative index $WL_x$. The moment of intersection between the two $|\Phi_x|$ distributions is marked with an arrow. This moment will be used in further analysis when ranking WUx and WLx indices for the modeled storms.

The process of development of our probabilistic predictive Pmodel is illustrated in Figures 4a–4h. Here the probability of occurrence (%) of the globally-distributed W-index (from +1 to +4 in the upper panels, and from −1 to −4 in the lower panels) is given. The probability distribution is calculated from the selected training set of GIM-WTEC maps for the time of $WU_{max}$ peak of the modeling storm on March 13, 1989, 12:00 UT. The probability of the frequency of occurrence of the W-index (%) is calculated for successive $\Phi_x$ ($n_i = 0, 1, \ldots, n - 1$) at each cell of the map from the nine training GIM-W maps, and is normalized relative to the total number of grids on the maps. The results shown in Figure 4 demonstrate that the probability of occurrence of different index levels differs both in magnitude and location.

Based on these probability maps (Pmodel) at different levels (such as those shown in Figure 4) we can draw up a combined global probability map of GIM-$W_x$ distribution for the desired values of $\Phi_x$ (such as Figure 3) for every storm in the SC22 modeling set. Given the storm phase distribution $\Phi_x$ for the selected SC22 storms, we can proceed to generate the probability maps (Pmodel), similar to those maps shown in Figure 4, for each value of $\Phi_x$ in the required storm model. The source GIM-W maps are selected for the calculation of Pmodel among the nearest values of $\Phi_i \approx \Phi_x$ (with $\Phi_i$ of the training set for $\Phi_x$ of the modeling set) of storms in each distribution WU($\Phi_i$) and WL($\Phi_i$) in the storm training set (shown in Figure 2). From Pmodel maps (Figure 4) we calculate the global maximum probability $P(W)_{max}$, the median $\mu(W)$ and the upper quartile $\psi(W)$ for indices at different levels ($W = \pm1, \pm2, \pm3, \pm4$).

Figure 4 illustrates the process of selecting a distribution of W-indices on the desired GIM-$W_x$ map as a function of the storm phase. Since many of the cells in the maps (e.g., as in Figure 4) refer to overlapping of the different W levels observed at a particular cell, it is necessary to restrict the reproduction of W-index in the cells with the different values of $P(W)$, %, in order to obtain the optimal distribution of W-indices of different levels on the desired GIM-$W_x$ map. This process is based on the set of maps of probability distribution (Pmodel), taking into account the most effective contribution of each level of the W-index at the individual map cells. Thus we proceed
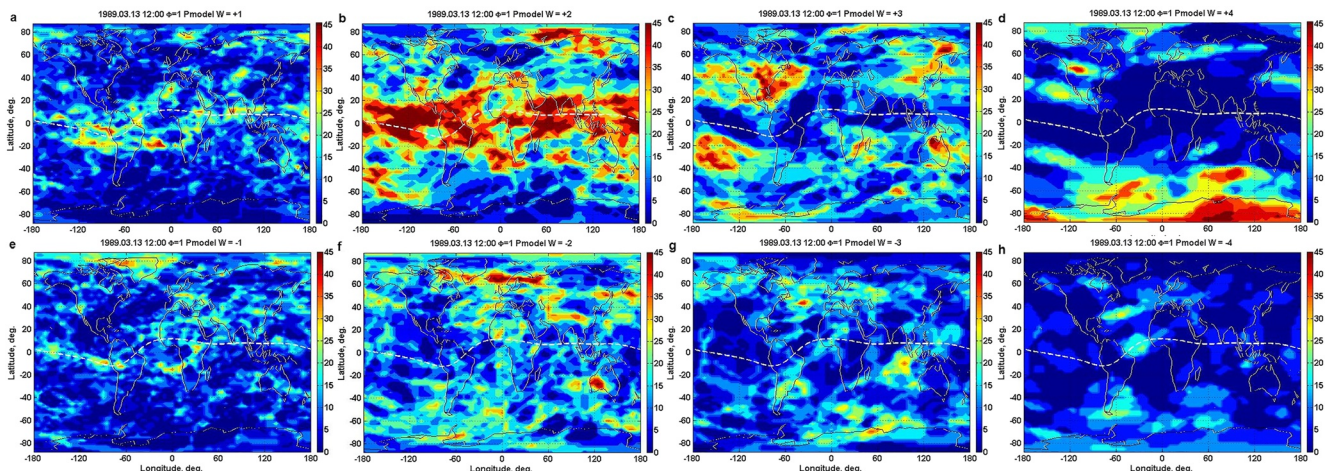


**Figure 4.** Probability of occurrence (%) of the globally distributed W index (from +1 to +4 in the upper panels, and from −1 to −4 in the lower panels) calculated from the training set of GIM-WTEC maps at peak of WUmax for the modeling super-storm on March 13, 1989, 12:00 UT.

**Table 3**
*Values of the Coefficient Used for Updating Monthly Median MTEC With the Instantaneous W Index to Produce the Instant Proxy TEC*

| W | −4 | −3 | −2 | −1 | 0 | 1 | 2 | 3 | 4 |
|---|---|---|---|---|---|---|---|---|---|
| $10^{DTEC}$ | 0.50 | 0.59 | 0.79 | 0.95 | 1.00 | 1.05 | 1.26 | 1.69 | 2.00 |

to ranking the Pmodel's results by their significance at different phases of the ionospheric storm.

The rank level of the proxy GIM-WTEC$_x$ map is calculated from the upper quartile $\psi(W)$ and the median $\mu(W)$ of probability $P(W)$ for each $W$ level ($W = \pm1, \pm2, \pm3, \pm4$) that exceeds the empirically-selected threshold:

$$\text{Tw}(W, \Phi) = \psi(W) \times (\psi(W) - \mu(W)) \times (1 - |\Phi_x|)/2 \qquad (3)$$

Here $\psi(W)$ is the upper quartile of probability $P(W)$, $\mu(W)$ is the median of $P(W)$, and $\Phi_x$ is the phase of a modeled storm. The threshold $\text{Tw}(W, \Phi)$ is deduced from the training set of storms by selecting a relevant GIM-W for the source $\Phi_i$ nearest to $\Phi_x$ of the modeled storm event.

The desired GIM-W$_x$ maps have a dominant positive WU-index with $P(W > 0) > \text{Tw}(W, \Phi)$ before reaching equality of the phase $\Phi_x(\text{WU}_x)$ and $|\Phi_x(\text{WL}_x)|$ (the example before the arrow in Figure 3). At this stage of a modeled storm, the first rank is assigned to $\text{Tw}_{max}(W > 0)$ for the probability of a positive W-index, while $\Phi_x(W > 0)$ exceeds $|\Phi_x(W < 0)|$. The second rank is detected for the rest W-indices with the same criteria, and a similar procedure is applied to determine the third and fourth ranks. After that the remaining cells on the desired GIM-W$_x$ map are filled with W-indices with $P(W > 0) > \text{Tw}(W, \Phi)$, followed with the four Pmodel distributions for the negative W-indices ranked by decrease in occurrence of $P(W < 0) > \text{Tw}(W, \Phi)$. The process is inverted using $\text{Tw}_{max}(W < 0)$ for the first rank, where $|\Phi(W < 0)|$ exceeds $|\Phi(W > 0)|$ after equality of the storm phases $\Phi_x(\text{WU}_x)$ to $|\Phi_x(\text{WL}_x)|$, starting with the dominant occurrence of $P(W < 0) > \text{Tw}(W, \Phi)$ for the negative set of indices, and so on. In total, we have a series of $\text{Tw}(W, \Phi)$ values, which we rank to compile the GIM-WTEC$_x$ composite map as they are decreasing in sub-sequences for the four maps $P(W > 0)$ and the four maps $P(W < 0)$.

Having the monthly median GIM-MTEC produced with MTEC model for each hour of the modeled storm (Table 2) and a model set of predicted GIM-W$_x$ maps, we can complete the process of reconstruction of the proxy maps GIM-TEC$_x$ for the extreme storms of SC22. The correction of the median MTEC value for an instantaneous GIM-TEC$_x$ map is performed using the calculated W$_x$ value at each cell of the map, according to the formula:

$$\text{TEC} = \text{MTEC} \times 10^{DTEC} \qquad (4)$$

This expression is deduced by inverting the expression for W index in dependence on the relevant logarithmic deviation DTEC from the median (Gulyaeva et al., 2021). The correction term, $10^{DTEC}$, expressed versus W-index is provided in Table 3.

The results of the application of the probabilistic Pmodel are shown in Figures 5a and 5c. Here the GIM-MTEC median map (Figure 5a), the GIM-W$_x$ proxy map (Figure 5b) and the GIM-TEC$_x$ proxy map (Figure 5c) are plotted for the peak of a positive phase of the super-storm on March 13, 1989 at 12:00 UT. The GIM-W$_x$ map is obtained with the proposed algorithm from the probability maps shown in Figure 4. It is observed that the instantaneous TEC$_x$ map differs significantly from the median MTEC map due to the positive response of electron content at the peak of the main phase of the ionospheric storm WU$_{max}$. The area of increased ionization is marked in red in Figure 5b with a dominant location at the auroral cap of the Southern Hemisphere. A moderate positive
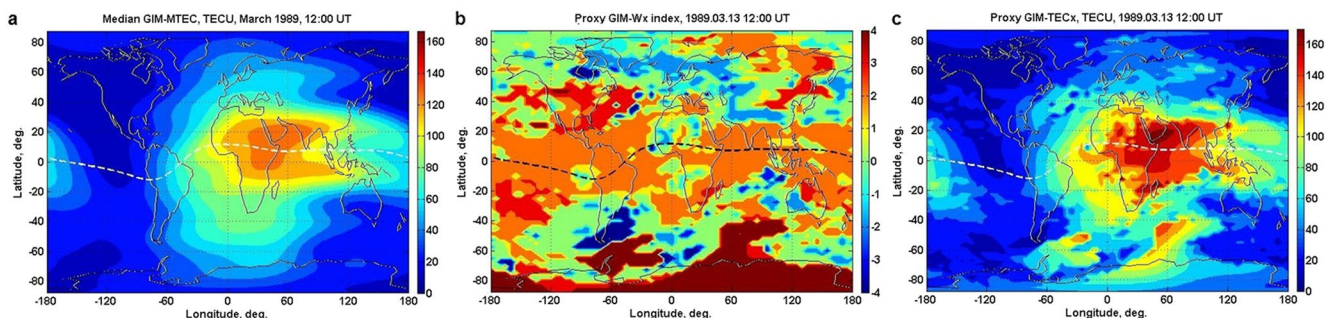


**Figure 5.** Global ionosphere maps produced for the peak of a positive phase of the super-storm on March 13, 1989 at 12:00 UT: (a) GIM-MTEC median map; (b) GIM-WTEC$_x$ proxy map; (c) GIM-TECx proxy map.
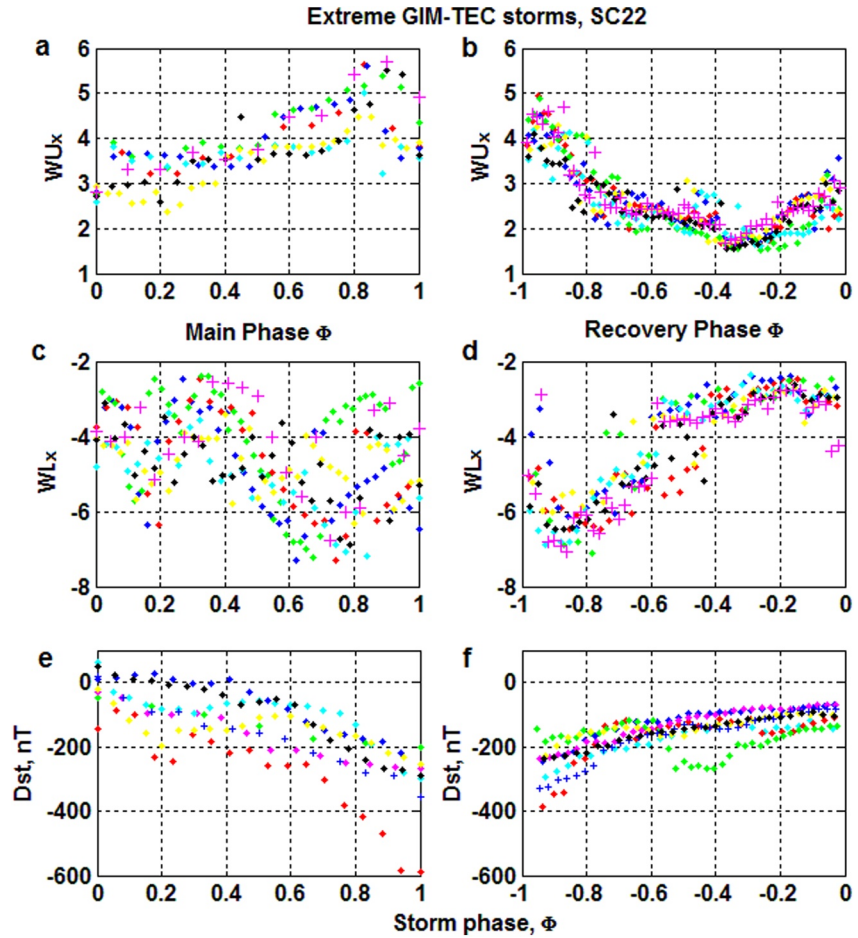
**Figure 6.** Variation of the ionospheric and geomagnetic global indices against the main phase and recovery phase of eight modeling storms of SC22 obtained from the proxy model GIM-W$_x$: (a, b) WU$_x$ ($\Phi$) index; (c, d) WL$_x$($\Phi$) index; (e, f) Dst($\Phi$) index.

disturbance ($W = 2$) is observed at the equatorial region. The reliability of the TEC proxy maps determination is validated in the next section.

The phase portrait of the modeled SC22 storms obtained from the proxy GIM-W$_x$ model is plotted in Figure 6 similar to the training storms (Figure 2). Here variation of the WU$_x$ indices (Figures 6a and 6b), the WL$_x$ indices (Figures 6c and 6d) and Dst indices (Figures 6e and 6f) are plotted as a function of the storm phase $\Phi_x$. This figure illustrates the similarity of variation of these parameters for all SC22 extreme events, including the main phase of growth for the positive WU$_x$ index (the decline for the negative WL$_x$ and Dst indices), and opposite trends for the recovery phase. The scatter of WL$_x$ values in the main phase is caused by a significant difference in the duration of this phase for the different SC22 events, which is revealed in the different onset of the GIM-W($\Phi_i$) maps in the process of constructing the predictive Pmodel($\Phi_x$).

## 4. Validation of Proxy GIM-TEC$_x$ With Four Intense Storms of SC23-SC24

Four additional SC23 and SC24 geomagnetic/ionospheric storms are used to demonstrate the model's performance for SC22 storms. The test set of storms is listed in Table 4. Here the storm onset $t_0$, the time and value of the peak of the Dst-index, the time of the peak of the positive ionosphere storm WU$_{max}$ and the negative storm WL$_{min}$ are listed. The 12-month sunspot number SSN2 is also provided. The Pmodel was developed for three days starting from 00:00 UT for the day of $t_0$, with a total duration of 72 h UT. GIM-W$_x$ and GIM-TEC$_x$ maps were calculated for the four testing storms using the proposed probabilistic Pmodel.

**Table 4**
*Testing Set of the Extreme Storms for SC23–SC24*

| Start year-mm-dd | UT | Dst_min mm-dd | UT | Dst | WU_max mm-dd | UT | WU | WL_min mm-dd | UT | WL | SSN |
|---|---|---|---|---|---|---|---|---|---|---|---|
| 1998-05-03 | 18:00 | 05-04 | 05:00 | −205 | 05-03 | 21:00 | 3.90 | 05-04 | 20:00 | −4.37 | 81 |
| 1998-09-25 | 00:00 | 09-25 | 09:00 | −207 | 09-25 | 06:00 | 2.70 | 09-25 | 08:00 | −4.43 | 96 |
| 2015-03-17 | 05:00 | 03-17 | 22:00 | −223 | 03-17 | 10:00 | 2.84 | 03-18 | 07:00 | −5.35 | 82 |
| 2015-06-22 | 19:00 | 06-23 | 04:00 | −204 | 06-22 | 21:00 | 4.90 | 06-23 | 17:00 | −3.11 | 72 |

The results of calculating the WUx and WLx indices (dashed blue and red curves, respectively) are plotted in Figure 7. These indices are compared with observed global WUg and WLg indices (solid blue and red curves) calculated from GIM-W maps representing the relative changes in the UQRG GIM-TEC with respect to the GIM-MTEC model. For comparison, the WU and WL global indices (black curves) are also shown, representing the relative changes of W-index of the observed UQRG GIM-TEC maps relative to the running −15days median. Insignificant differences are observed between WUg and WLg results compared with WU and WL. However, predicted amplitudes of both positive and negative phases of the storms ($WU_x$ and $WL_x$) exceed the 'true' values. This may be due to more intense training storms (Dst < −250 nT) used for reconstruction of the testing storms ($WU_x$ and $WL_x$) compared to the intensity of the testing set (Dst < −200 nT): the original WU and WL indices for the SC23 training set are greater (affecting the increased $WU_x$ and $WL_x$ results) than those observed WU and WL for the testing set.

JPL GIM-TEC and UPC GIM-TEC hourly maps are selected for validation of the proxy $GIM\text{-}TEC_x$ maps with observed data. The root-mean-square error of the $GIM\text{-}TEC_x$ proxy is calculated as follows:

$$\text{RMSE} = \sqrt{\frac{1}{N} \sum_{n=1}^{N} \left( TEC_n^{obs} - TEC_n^{mod} \right)^2} \qquad (5)$$

Here $TEC^{obs}$ means TEC_UPC or TEC_JPL, $TEC^{mod} = TEC_x$, and N is the number of value pairs to compare.
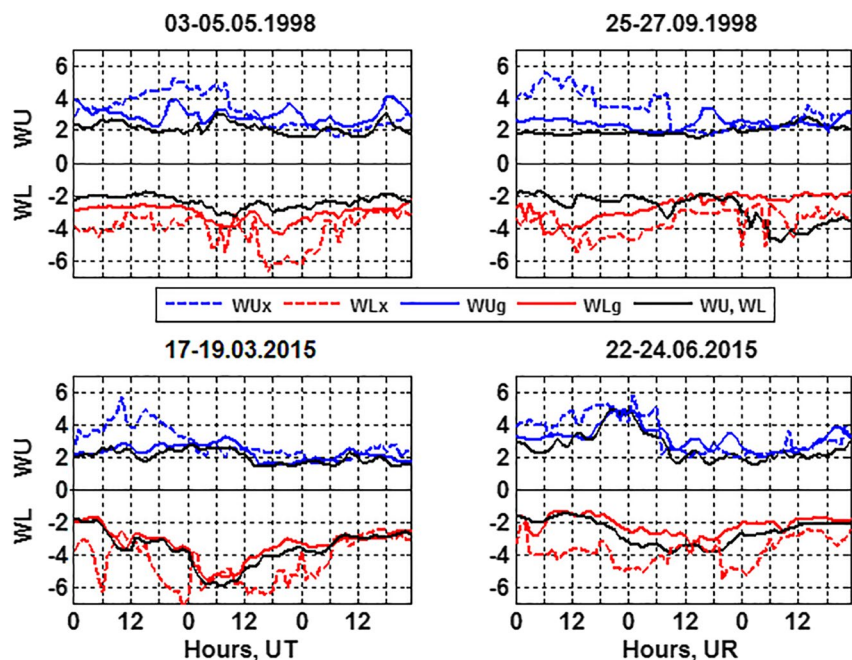


**Figure 7.** Temporal variation of positive ionosphere global WU index and negative WL index for four ionospheric testing storms: (1) results of proxy WUx; and WLx; indices; (2) data-model based WUg and WLg indices relative to global median MTEC model; (3) observed WU and WL global indices relative to the running median for the preceding 15 days.

**Table 5**
*Daily RMSE (TECU) Between the Proxy GIM-TECx and Observed JPL GIM-TEC and UPC GIM-TEC Data During Three Days for Four Testing Intense Storm Events of SC23 and SC24*

| Event | Date | JPL | UPC |
|---|---|---|---|
| 1 | 1998-05-03 | 1.58 | 1.92 |
|  | 1998-05-04 | 1.96 | 2.46 |
|  | 1998-05-05 | 1.38 | 1.76 |
| 2 | 1998-09-25 | 1.38 | 3.04 |
|  | 1998-09-26 | 1.38 | 1.79 |
|  | 1998-09-27 | 1.40 | 1.76 |
| 3 | 2015-03-17 | 2.48 | 2.85 |
|  | 2015-03-18 | 2.28 | 2.60 |
|  | 2015-03-19 | 1.80 | 2.12 |
| 4 | 2015-06-22 | 1.47 | 1.56 |
|  | 2015-06-23 | 1.26 | 1.62 |
|  | 2015-06-24 | 0.98 | 1.16 |

The results listed in Table 5 for selected GIM-TEC data are combined for all UT hourly values 0, 1, …, 23 h for a given day. Each map in IONEX format (Schaer, 1999) includes 5183 cells. Hence, the total number of pairs of values to compare in Table 5 for a 24 h period is $N = 5183 * 24 = 124,392$. It follows from Table 5 that the accuracy of our GIM-TEC$_x$ predictions compared to JPL maps is less than 2.5 TECU and for UPC maps is less than 3.1 TECU. The UPC RMSE is greater than that of JPL because the median model MTEC is built on JPL data and the two GIM-TECs show differences (Shubin & Gulyaeva, 2022). Day-to-day difference of RMSE is observed for all events. These results show that the TEC reconstruction error is significantly below the standard deviation of the observed GIM-TEC maps from the altimeter measurements for high solar activity, which show VTEC STD values that varied from 3.61 to 5.97 TECU during 2014 (Wielgosz et al., 2021).

## 5. Conclusions

A technique for reconstructing the instantaneous global ionosphere maps of total electron content (GIM-TECx) is developed. It is applied for eight SC22 extreme storms in order to produce the instantaneous hourly maps GIM-W$_x$ and GIM-TEC$_x$ for the epoch before GNSS global mapping. The method is based on the analysis of ionosphere GIM-W index maps, which are calculated as the logarithmic deviation of 15-min UPC GIM-TEC (UQRG) observations from the median GIM-MTEC model.

For the first time in the literature, a phase portrait of the ionospheric and geomagnetic storm is constructed that includes main and recovery phases for the positive ionosphere disturbance (the WU-index), the negative disturbance (the WL-index), and the ring current (the Dst-index). To predict GIM-W$_x$ for SC22, a similar phase dependence $\Phi(W)$ for simulated events is calculated, with the time of the peak WU$_{max}$ and the peak WL$_{min}$ determined from the probable time lag of the ionospheric storm's peaks relative to the Dst peak.

A probabilistic forecasting model (Pmodel) for the GIM-W$_x$ ionospheric index is developed. The model consists of probability maps for various levels of the W-index (from −4 to −1 for decreasing electron content and from +1 to +4 for increasing ionization). This is based on the analysis of GIM-W maps for a training set of nine extreme ionospheric-geomagnetic storms in SC23 with Dst < −250 nT. An application of the proposed Pmodel may be expanded in the future with increased training database by incorporating additional major storms in the GNSS age.

In particular, Equations 1a and 1b constitute a crucial time difference between the time of Dst$_{min}$ and the time of the ionosphere storm peaks but they don't include seasonal effects of the different signs of the storm. However, the seasonal differences could not be evaluated in the framework of the present study due to limited number of the extreme events. Only three equinox events in the training set, two events in the testing set, and five events in the modeling set are available. The rest events refer to the summer and winter conditions which evaluation would require separating the ionosphere state in the Northern and Southern hemispheres for the opposite winter/summer seasons, that is., separate evaluation of WU and WL indices for two of the half a sphere for the proposed global probability Pmodel. We believe that the season effects could be resolved in the future study which could include more than 100 intense training storms with Dst < −100 nT during 1996–2021.

The final GIM-W$_x$ proxy map is generated by ranking the Pmodel depending on the phase $\Phi(W)$ of the ionospheric storm according to a specified threshold Tw($\Phi$,W) of the probability of W-index occurrence in the cells of the GIM-W$_x$ map. The procedure ends with the production of the instantaneous GIM-TECx proxy map by adjusting the GIM-MTEC median map to the GIM-W$_x$ prediction.

A comparison of the probabilistic model with data for four intense ionospheric storms in SC23 and SC24 exhibits a GIM-TECx RMSE less than three TECU as compared with the JPL GIM-TEC and UPC GIM-TEC maps. This innovative probabilistic model can be applied to both the reconstruction of historical GIM-TEC and current real time forecasting.

## Data Availability Statement

The GIM-TEC data are openly accessible from the UPC server (https://upc_ionex/YEAR/DOY_YYM-MDD.15min/uqrgDOY0.YYi.Z), and JPL server https://sideshow.jpl.nasa.gov/pub/iono_daily/. Dst data can be accessed from http://wdc.kugi.kyoto-u.ac.jp/dstdir/index.html. The GIM-W index maps and catalogues of ionospheric and geomagnetic storms are available at http://www.izmiran.ru/ionosphere/weather/.

## References

Aa, E., Zhang, D., Ridley, A. J., Xiao, Z., & Hao, Y. (2012). A global model: Empirical orthogonal function analysis of total electron content 1999–2009 data. *Journal of Geophysical Research A: Space Physics*, *117*(A3). https://doi.org/10.1029/2011ja017238

Beutler, G., Moore, A. W., & Mueller, I. I. (2009). The international global navigation satellite systems service (IGS): Development and achievements. *The Journal of Geodesy*, *83*, 297–307. https://doi.org/10.1007/s00190-008-0268-z

Bilitza, D., Altadill, D., Truhlik, V., Shubin, V., Galkin, I., Reinisch, B., & Huang, X. (2017). International Reference Ionosphere 2016: From ionospheric climate to real-time weather predictions. *Space Weather*, *15*, 418–429. https://doi.org/10.1002/2016SW001593

Cesaroni, C., Spogli, L., Aragon-Angel, A., Fiocca, M., Dear, V., De Franceschi, G., & Romano, V. (2020). Neural network based model for global Total Electron Content forecasting. *Journal of Space Weather and Space Climate*, *10*, 11. https://doi.org/10.1051/swsc/2020013

Chasovitin, Y. K., Shirochkov, A. V., Besprozvannaya, A. S., Gulyaeva, T. L., Denisenko, P. F., Armenskaya, O. A., et al. (1987). An empirical model for the global distribution of density, temperature and effective collision frequency of electrons in the ionosphere. *Advances in Space Research*, *7*(6), 49–52. https://doi.org/10.1016/0273-1177(87)90270-5

Chen, Z., Zhang, S.-R., Coster, A. J., & Fang, G. (2015). EOF analysis and modeling of GPS TEC climatology over North America. *Journal of Geophysical Research A: Space Physics*, *120*(4), 3118–3129. https://doi.org/10.1002/2014ja020837

Erdogan, E., Schmidt, M., Goss, A., Görres, B., & Seitz, F. (2020). Adaptive modeling of the global ionosphere vertical total electron content. *Remote Sensing*, *12*, 1822. https://doi.org/10.3390/rs12111822

Feltens, J. (2003). The international GPS service (IGS) ionosphere working group. *Advances in Space Research*, *31*(3), 635–644. https://doi.org/10.1016/s0273-1177(03)00029-2

Feng, J. F., Han, B., Zhao, Z., & Wang, Z. (2019). A new global total electron content empirical model. *Remote Sensing*, *11*, 706. https://doi.org/10.3390/rs11060706

Galkin, I. A., Reinisch, B. W., Vesnin, A. M., Bilitza, D., Fridman, S., Habarulema, J. B., & Veliz, O. (2020). Assimilation of sparse continuous near-earth weather measurements by NECTAR model morphing. *Space Weather*, *18*, e2020SW002463. https://doi.org/10.1029/2020SW002463

Goncharenko, L. P., Tamburri, C. A., Tobiska, W. K., Schonfeld, S. J., Chamberlin, P. C., Woods, T. N., et al. (2021). A new model for ionospheric total electron content: The impact of solar flux proxies and indices, *Journal of Geophysical Research A: Space Physics*, *126*(2), e28466. https://doi.org/10.1029/2020JA028466

Gulyaeva, T. L. (1999). Regional analytical model of ionospheric total electron content: Monthly mean and standard deviation. *Radio Science*, *34*, 1507–1512. https://doi.org/10.1029/1999rs900080

Gulyaeva, T. L., Arikan, F., Hernández-Pajares, M., & Stanislawska, I. (2013). GIM-TEC adaptive ionospheric weather assessment and forecast system. *The Journal of Atmospheric and Solar-Terrestrial Physics*, *102*, 329–340. https://doi.org/10.1016/j.jastp.2013.06.011

Gulyaeva, T. L., Haralambous, H., & Stanislawska, I. (2021). Persistent perturbations of ionosphere at diminution of solar and geomagnetic activity during 21–24 solar cycles. *The Journal of Atmospheric and Solar-Terrestrial*, *221*. 105706. https://doi.org/10.1016/j.jastp.2021.105706

Gulyaeva, T. L., & Mannucci, A. J. (2020). Echo of ring current storms in the ionosphere. *The Journal of Atmospheric and Solar-Terrestrial*, *205*, 105300. https://doi.org/10.1016/j.jastp.2020.105300

Hernández-Pajares, M., Juan, J., & Sanz, J. (1999). New approaches in global ionospheric determination using ground GPS data. *The Journal of Atmospheric and Solar-Terrestrial Physics*, *61*, 1237–1247. https://doi.org/10.1016/S1364-6826(99)00054-1

Hernández-Pajares, M., Juan, J., Sanz, J., Orús, R., García-Rigo, A., Feltens, J., & Krankowski, A. (2009). The IGS VTEC maps: A reliable source of ionospheric information since 1998. *The Journal of Geodesy*, *83*(3–4), 263–275.

Ivanov, V. B., Gefan, G. D., & Gorbachev, O. A. (2011). Global empirical modelling of the total electron content of the ionosphere for satellite radio navigation systems. *The Journal of Atmospheric and Solar-Terrestrial*, *73*(13), 1703–1707. https://doi.org/10.1016/j.jastp.2011.03.010

Jakowski, N., Mayer, C., Hoque, M. M., & Wilken, V. (2011). Total electron content models and their use in ionosphere monitoring. *Radio Science*, *46*(6). https://doi.org/10.1029/2010rs004620

Lean, J. L. (2019). One- to 10-day forecasts of ionospheric total electron content using a statistical model. *Space Weather*, *17*(2), 313–338. https://doi.org/10.1029/2018sw002077

Lean, J. L., Meier, R. R., Picone, J. M., Sassi, F., Emmert, J. T., & Richards, P. G. (2016). Ionospheric total electron content: Spatial patterns of variability, *Journal of Geophysical Research A: Space Physics*, *121*(10), 10367–10402, https://doi.org/10.1002/2016JA023210

Liu, Q., Hernández-Pajares, M., Lyu, H., & Goss, A. (2021). Infuence of temporal resolution on the performance of global ionospheric maps. *The Journal of Geodesy*, *95*(34), 34. https://doi.org/10.1007/s00190-021-01483-y

Liu, Q., Hernández-Pajares, M., Lyu, H., Nishioka, M., Yang, H., Monte-Moreno, E., et al. (2021). Ionospheric storm scale index based on high time resolution UPC-IonSAT global ionospheric maps (IsUG). *Space Weather*, *19*, e2021SW002853. https://doi.org/10.1029/2021SW002853

Liu, Q., Hernández-Pajares, M., Yang, H., Monte-Moreno, E., Roma-Dollase, D., García-Rigo, A., et al. (2021). The cooperative IGS RT-GIMs: A global and accurate estimation of the ionospheric electron content distribution in real-time. *Earth System Science Data*, *13*(9), 4567–4582. https://doi.org/10.5194/essd-13-4567-2021

Liu, L., Zou, A., Yao, Y., & Wang, Z. (2020). Forecasting global ionospheric TEC using deep learning approach. *Space Weather*, *18*, e2020SW002501. https://doi.org/10.1029/2020SW002501

Li, Z., Wang, N., Hernández-Pajares, M., Yuan, Y., Krankowski, A., Liu, A., et al. (2020). IGS real-time service for global ionospheric total electron content modeling. *The Journal of Geodesy*, *94*, 32. https://doi.org/10.1007/s00190-020-01360-0

Love, J. J., Rigler, E. J., Pulkkinen, A., & Riley, P. (2015). On the lognormality of historical magnetic storm intensity statistics: Implications for extreme-event probabilities. *Geophysical Research Letters*, *42*, 6544–6553. https://doi.org/10.1002/2015GL064842

Meng, X., & Verkhoglyadova, O. P. (2021). Quantifying contributions of external drivers to the global ionospheric state. *Space Weather*, *19*, e2021SW002752. https://doi.org/10.1029/2021SW002752

Milanowska, B., Wielgosz, P., Krypiak-Gregorczyk, A., & Jarmołowski, W. (2021). Accuracy of global ionosphere maps in relation to their time interval. *Remote Sensing*, *13*, 3552. https://doi.org/10.3390/rs13183552

Monte Moreno, E., García Rigo, A., Hernández-Pajares, M., & Yang, H. (2018). TEC forecasting based on manifold trajectories. *Remote Sensing*, *10*(7), 988. https://doi.org/10.3390/rs10070988

Mukhtarov, P., Andonov, B., & Pancheva, D. (2013). Global empirical model of TEC response to geomagnetic activity. *Journal of Geophysical Research A: Space Physics*, *118*(10), 6666–6685. https://doi.org/10.1002/jgra.50576

Mukhtarov, P., Pancheva, D., Andonov, B., & Pashova, L. (2013). Global TEC maps based on GNSS data: 1. Empirical background TEC model. *Journal of Geophysical Research A: Space Physics*, *118*(7), 4594–4608. https://doi.org/10.1002/jgra.50413

Nava, B., Coisson, P., & Radicella, S. M. (2008). A new version of the NeQuick ionosphere electron density model. *The Journal of Atmospheric and Solar-Terrestrial Physics*, *70*(15), 1856–1862. https://doi.org/10.1016/j.jastp.2008.01.015

Orús, R., Hernández-Pajares, M., Juan, J. M., & Sanz, J. (2005). Improvement of global ionospheric VTEC maps by using kriging interpolation technique. *The Journal of Atmospheric and Solar-Terrestrial Physics*, *67*(16), 1598–1609. https://doi.org/10.1016/j.jastp.2005.07.017

Pignalberi, A., Habarulema, J. B., Pezzopane, M., & Rizzi, R. (2019). On the development of a method for updating an empirical climatological ionospheric model by means of assimilated vTEC measurements from a GNSS receiver network. *Space Weather*, *17*, 1131–1164. https://doi.org/10.1029/2019SW002185

Ratovsky, K. G., Klimenko, M. V., Yasyukevich, Y. V., Klimenko, V. V., & Vesnin, A. M. (2020). Statistical analysis and interpretation of high-, mid- and low-latitude responses in regional electron content to geomagnetic storms. *Atmosphere*, *11*, 1308. https://doi.org/10.3390/atmos11121308

Schaer, S. (1999). Mapping and predicting the Earth's ionosphere using the global positioning system (Ph.D. thesis). University of Berne.

Shubin, V. N., & Gulyaeva, T. L. (2021). Solar forcing on the ionosphere: Global model of the F2 layer peak parameters driven by re-calibrated sunspot numbers. *Acta Astronautica*, *179*, 197–208. https://doi.org/10.1016/j.actaastro.2020.10.029

Shubin, V. N., & Gulyaeva, T. L. (2022). Global mapping of Total Electron Content from GNSS observations for updating IRI-Plas model. *Advances in Space Research*. *69*(1), 168–175. https://doi.org/10.1016/j.asr.2021.09.032

Stanislawska, I., Gulyaeva, T. L., Grynyshyna-Poliuga, O., & Pustovalova, L. V. (2018). Ionospheric weather during five extreme geomagnetic superstorms since IGY deduced with the instantaneous global maps GIM-foF2. *Space Weather*, *16*(12), 2068–2078. https://doi.org/10.1029/2018SW001945

Wielgosz, P., Milanowska, B., Krypiak-Gregorczyk, A., & Jarmołowski, W. (2021). Validation of GNSS-derived global ionosphere maps for different solar activity levels: Case studies for years 2014 and 2018. *GPS Solutions*, *25*, 103. https://doi.org/10.1007/s10291-021-01142-x